Title

ATF7IP2/MCAF2 directs H3K9 methylation and meiotic gene regulation in the male germline

Journal

Genes & Development, 38(3-4)

ISSN

0890-9369

Authors

Alavattam, Kris G

Esparza, Jasmine M

Hu, Mengwen

et al.

Publication Date

2024-02-01

DOI

10.1101/gad.351569.124

ATF7IP2/MCAF2 directs H3K9 methylation and meiotic gene regulation in the male germline

Kris G. Alavattam,[1,2,8] Jasmine M. Esparza,[3,8] Mengwen Hu,[1,3,8] Ryuki Shimada,[4,8] Anna R. Kohrs,[1] Hironori Abe,[1,3,4] Yasuhisa Munakata,[1,3] Kai Otsuka,[3] Saori Yoshimura,[4] Yuka Kitamura,[3] Yu-Han Yeh,[1,3] Yueh-Chiang Hu,[1,5] Jihye Kim,[6] Paul R. Andreassen,[5,7] Kei-ichiro Ishiguro,[4] and Satoshi H. Namekawa[1,3,5]

[1]Reproductive Sciences Center, Division of Developmental Biology, Cincinnati Children's Hospital Medical Center, Cincinnati, Ohio 45229, USA; [2]Basic Sciences Division, Fred Hutchinson Cancer Center, Seattle, Washington 98109, USA; [3]Department of Microbiology and Molecular Genetics, University of California, Davis, Davis, California 95616, USA; [4]Department of Chromosome Biology, Institute of Molecular Embryology and Genetics (IMEG), Kumamoto University, Kumamoto 860-0811, Japan; [5]Department of Pediatrics, University of Cincinnati College of Medicine, Cincinnati, Ohio 49229, USA; [6]Laboratory of Chromosome Dynamics, Institute of Molecular and Cellular Biosciences, University of Tokyo, Tokyo 113-0032, Japan; [7]Division of Experimental Hematology and Cancer Biology, Cincinnati Children's Hospital Medical Center, Cincinnati, Ohio 45229, USA

H3K9 trimethylation (H3K9me3) plays emerging roles in gene regulation, beyond its accumulation on pericentric constitutive heterochromatin. It remains a mystery why and how H3K9me3 undergoes dynamic regulation in male meiosis. Here, we identify a novel, critical regulator of H3K9 methylation and spermatogenic heterochromatin organization: the germline-specific protein ATF7IP2 (MCAF2). We show that in male meiosis, ATF7IP2 amasses on autosomal and X-pericentric heterochromatin, spreads through the entirety of the sex chromosomes, and accumulates on thousands of autosomal promoters and retrotransposon loci. On the sex chromosomes, which undergo meiotic sex chromosome inactivation (MSCI), the DNA damage response pathway recruits ATF7IP2 to X-pericentric heterochromatin, where it facilitates the recruitment of SETDB1, a histone methyltransferase that catalyzes H3K9me3. In the absence of ATF7IP2, male germ cells are arrested in meiotic prophase I. Analyses of ATF7IP2-deficient meiosis reveal the protein's essential roles in the maintenance of MSCI, suppression of retrotransposons, and global up-regulation of autosomal genes. We propose that ATF7IP2 is a downstream effector of the DDR pathway in meiosis that coordinates the organization of heterochromatin and gene regulation through the spatial regulation of SETDB1-mediated H3K9me3 deposition.

[*Keywords*: meiosis; constitutive heterochromatin; H3K9me3; meiotic sex chromosome inactivation; gene activation; ATF7IP2/MCAF2]

Supplemental material is available for this article.

Received September 30, 2023; revised version accepted January 31, 2024.

Constitutive heterochromatin forms mainly at pericentromeres and is maintained to ensure genome stability. A hallmark of constitutive heterochromatin is histone H3K9 trimethylation (H3K9me3) (Saksouk et al. 2015). It was initially considered a static histone mark due to its stable accumulation on tandem satellite repeats at pericentric heterochromatin (PCH); however, a growing literature reveals that H3K9me3—particularly H3K9me3 mediated by the histone methyltransferase SETDB1—has broad, dynamic roles in suppressing developmental regulator genes and endogenous retroviruses in embryonic stem cells (Bilodeau et al. 2009; Matsui et al. 2010), thereby defining cellular identities in somatic development (Becker et al. 2016; Nicetto and Zaret 2019).

An essential factor in the germline, SETDB1 is required for gene regulation, the suppression of transposable elements (TEs), and the control of meiotic chromosome behavior (Liu et al. 2014; Hirota et al. 2018; Mochizuki et al. 2018; Cheng et al. 2021). The redundant H3K9me3 methyltransferases SUV39H1 and SUV39H2 are also required for male meiosis (Peters et al. 2001). Thus, the

[8]**These authors contributed equally to this work.**
Corresponding authors: snamekawa@ucdavis.edu, ishiguro@kumamoto-u.ac.jp
Article published online ahead of print. Article and publication date are online at http://www.genesdev.org/cgi/doi/10.1101/gad.351569.124.

regulation of H3K9me3 is critical in male meiosis, where constitutive heterochromatin is remodeled to undergo synapsis and meiotic recombination on homologous chromosomes (Scherthan et al. 2014; Berrios 2017; Maezawa et al. 2018a). However, it remains a mystery why and how H3K9me3 undergoes dynamic regulation in male meiosis.

In addition to its roles at PCH, H3K9me3 is subject to dynamic temporal and spatial regulation on the male sex chromosomes as they undergo meiotic sex chromosome inactivation (MSCI) (Turner 2015; Alavattam et al. 2022). An essential event in the male germline, MSCI is initiated and maintained by a DNA damage response (DDR) pathway (Ichijima et al. 2011; Royo et al. 2013; Abe et al. 2022). Downstream from the DDR, SETDB1 establishes H3K9me3 on the sex chromosome and regulates MSCI (Hirota et al. 2018). SETDB1 is expressed in a broad range of cells, but there is a major knowledge gap as to how SETDB1 and H3K9me3 function in meiosis.

Here, we identify activating transcription factor 7-interacting protein 2 (ATF7IP2), also known as MBD1-containing chromatin-associated factor 2 (MCAF2), as a novel, critical regulator of SETDB1's spatiotemporal activity, H3K9 methylation, and global spermatogenic gene regulation. We identified ATF7IP2 based on its gene expression in the germline. In the midst of our investigation, an IP-mass spectrometry analysis identified ATF7IP2 as a SETDB1-binding protein (Hirota et al. 2018), lending the factor further contextual significance. In mitotically cycling cells, its homolog, ATF7IP (MCAF1), regulates SETDB1 for H3K9me3 establishment and transcriptional silencing (Ichimura et al. 2005; Timms et al. 2016; Tsusaka et al. 2019, 2020). We show that ATF7IP2 is a counterpart to ATF7IP that is highly expressed in the germline and is essential in male meiosis, revealing roles for ATF7IP2 in MSCI, global meiotic gene regulation, and the fine-tuning of retrotransposon-derived loci such as endogenous retroviruses. By uncovering ATF7IP2's germline functions, our study clarifies the regulatory logic for dynamic H3K9me3 deposition—and thus heterochromatin—in the male germline.

Results

ATF7IP2 is highly expressed in male meiosis and accumulates on heterochromatin

To understand the meiosis-specific regulation of H3K9me3, we focused on *Atf7ip2* (*Mcaf2*), a gene that is highly expressed in male meiosis, as evidenced in RNA-seq data sets for germ cell development and spermatogenesis (Fig. 1A; Seisenberger et al. 2012; Hasegawa et al. 2015; Maezawa et al. 2018b). *Atf7ip2* expression is low in male germ cells until the stage of meiosis, at which point it is highly up-regulated in meiotic pachytene spermatocytes (Fig. 1A). On the other hand, its homolog, *Atf7ip* (*Mcaf1*), which functions in mitotically dividing/somatic cells (Ichimura et al. 2005; Timms et al. 2016), is highly expressed in primordial germ cells and spermatogonia but is down-regulated in pachytene spermatocytes. Among various tissues, *Atf7ip2* is highly expressed in testes (Supplemental Fig. S1A). Furthermore, mouse ATF7IP2 has high homology with human ATF7IP2 (Supplemental Fig. S1B), except for its long N-terminal amino acid tail, and ATF7IP2 is highly expressed in the meiotic spermatocytes of human testes (Supplemental Fig. S1C). These results raise the possibility that ATF7IP2 is an evolutionarily conserved counterpart to ATF7IP that is highly expressed in late stages of spermatogenesis.

To understand the regulatory mechanism for *Atf7ip2* expression, we examined the genomic distribution of MEIOSIN and STRA8, both transcription factors that heterodimerize to initiate meiosis-specific transcription (Kojima et al. 2019; Ishiguro et al. 2020). We observed MEIOSIN and STRA8 peaks at the *Atf7ip2* transcription start site (TSS) in preleptotene-enriched testes (the preleptotene stage is a liminal stage for germ cells transitioning from mitosis to meiotic prophase I) (Fig. 1B, which is a reanalysis of data from Ishiguro et al. 2020). These peaks coincide with the accumulation of RNA polymerase II (POLII) and cap analysis of gene expression (CAGE) signals in postnatal day 10.5 (P10.5) testes, which are enriched for preleptotene spermatocytes (Fig. 1B, which is a reanalysis of data from Li et al. 2013). In support of a role for MEIOSIN and STRA8 in *Atf7ip2* expression, *Atf7ip2* was down-regulated in *Stra8*$^{-/-}$ and *Meiosin*$^{-/-}$ testes at P21 (Fig. 1C). In mouse testes, the first wave of meiosis occurs semisynchronously, and *Atf7ip2* expression is at its highest in P18 testes, when late stages of meiotic prophase I spermatocytes first appear (Fig. 1C). Taken together, these results demonstrate that the expression of *Atf7ip2* is up-regulated by MEIOSIN and STRA8, occurring amid a broad range of meiotic transcription (Kojima et al. 2019; Ishiguro et al. 2020).

To better understand the potential function of ATF7IP2, we investigated ATF7IP2 protein localization during stages of mouse male meiosis by performing immunofluorescence microscopy with chromosome spreads (Fig. 1D,E). In the leptotene stage of meiotic prophase I, when meiotic chromosome axes begin to condense, ATF7IP2 localizes on DAPI-discernible heterochromatin. ATF7IP2 continues to localize on all DAPI-discernible PCH through the zygotene stage, when homologs undergo synapsis; the pachytene stage, when homologs have completed synapsis; and the diplotene stage, when homologs begin desynapsis (Fig. 1E). Meiotic nuclei were staged through observations of chromosome axes as identified by SYCP3 (Alavattam et al. 2016, 2018), a component of meiotic axes, and the presence of the testis-specific histone variant H1T, which appears in mid-pachytene nuclei and persists into haploid spermatids (Inselman et al. 2003). At the onset of the pachytene stage, the unsynapsed sex chromosomes undergo MSCI, and the most intense ATF7IP2 signals were observed on X-chromosome PCH (X-PCH) at that time (Fig. 1E,F). In the early and mid-pachytene stages, ATF7IP2 localizes primarily on X-PCH; from the late pachytene stage onward, ATF7IP2 gradually spreads across the entirety of the sex chromosome domain (also referred to as the "XY domain" or "XY chromatin"). Thus, ATF7IP2 exhibits two distinct

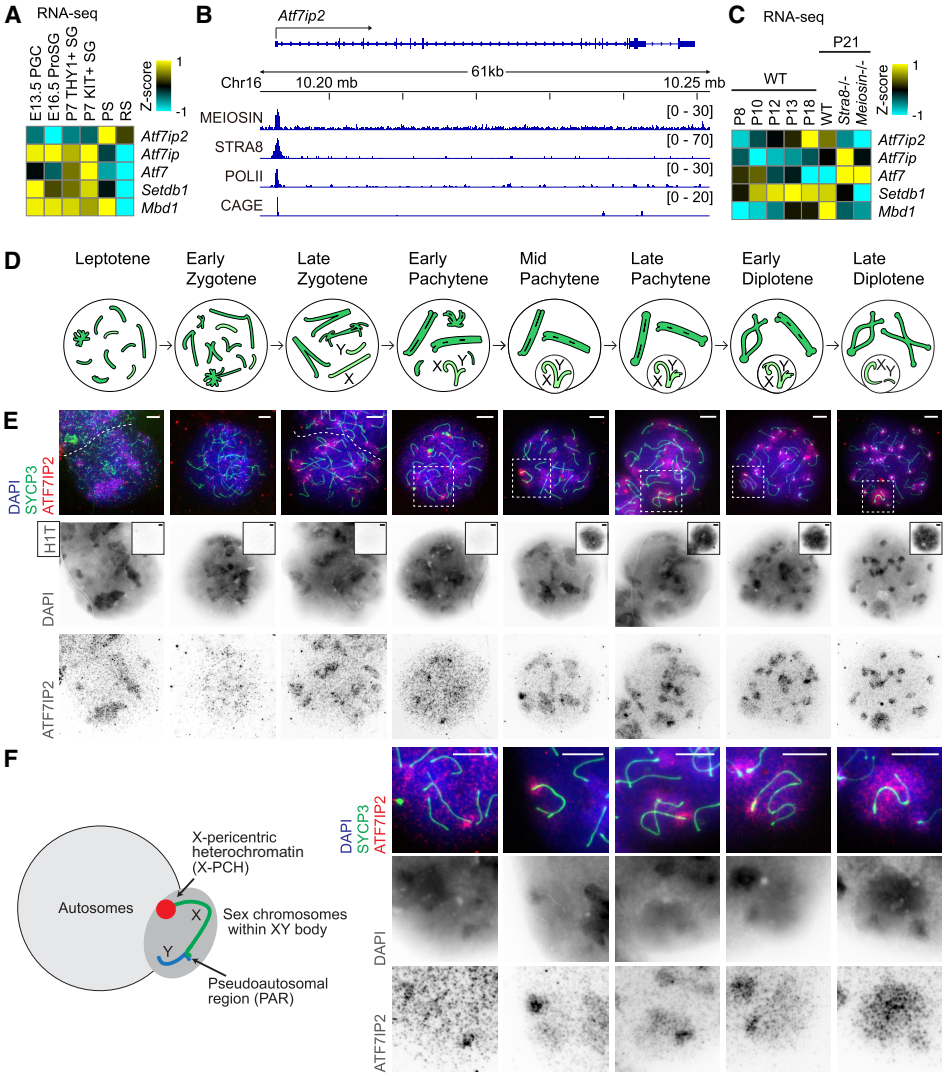

Figure 1. ATF7IP2 is highly expressed in male meiosis and accumulates on heterochromatin. (*A*,*C*) Heat maps showing bulk RNA-seq gene expression levels across a male germline time course for *Atf7ip2* and related genes. (PGC) Primordial germ cells, (ProSG) prospermatogonia, (SG) spermatogonia, (PS) pachytene spermatocytes, (RS) round spermatids. Original data for *A* are from Seisenberger et al. (2012), Hasegawa et al. (2015), and Maezawa et al. (2018b), and original data for *C* are from Ishiguro et al. (2020). (*B*) Track views for MEIOSIN (preleptotene-enriched testes), STRA8 (preleptotene-enriched testes), and RNA polymerase II (POLII; postnatal day 10.5 [P10.5] testes) ChIP-seq data and for CAGE (P10.5 testes). Numbers in brackets indicate ranges of normalized coverage. (*D*) Schematic of chromosome behavior in meiotic prophase I of male *Mus musculus*. (Darker green) Autosomes, (lighter green) sex chromosomes. (*E*) Meiotic chromosome spreads stained with DAPI and antibodies raised against ATF7IP2, SYCP3, and H1T; spreads represent stages of meiotic prophase I. (*Insets*) H1T immunostaining; H1T is a nuclear marker that appears in mid-pachytene nuclei and persists into haploid spermatids. SYCP3 is a marker of meiotic chromosome axes. Dashed squares are magnified in *F*. Scale bars, 5 µm. (*F*, *left*) Schematic of sex chromosome configuration in male meiosis. (*Right*) Magnified images of sex chromosomes from *E*. Scale bars, 5 µm.

localization patterns in meiotic prophase I: One is on the PCH of all chromosomes, and the other is intense accumulation on X-PCH that proceeds to spread through the entirety of the XY chromatin.

ATF7IP2 is required for male meiosis

To test the function of ATF7IP2, we performed CRISPR-mediated genome editing to generate *Atf7ip2* knockout mice. We targeted a guide RNA to a site within exon 4 (Fig. 2A), which encodes a portion of the SETDB1-binding domain (SETDB1-BD) that is conserved between ATF7IP2 and ATF7IP (Fig. 2B). We obtained three alleles with deletion lengths of 17, 31, and 169 bp. All caused *Atf7ip2* frameshift mutations, and all three homozygous *Atf7ip2* mutants displayed consistent and obvious testicular defects. For subsequent analyses, we selected the 17-bp deletion allele as a representative; hereafter, the homozygous 17-bp allele model is denoted as *Atf7ip2*$^{-/-}$. *Atf7ip2*$^{-/-}$ male mice were viable but infertile and had much smaller

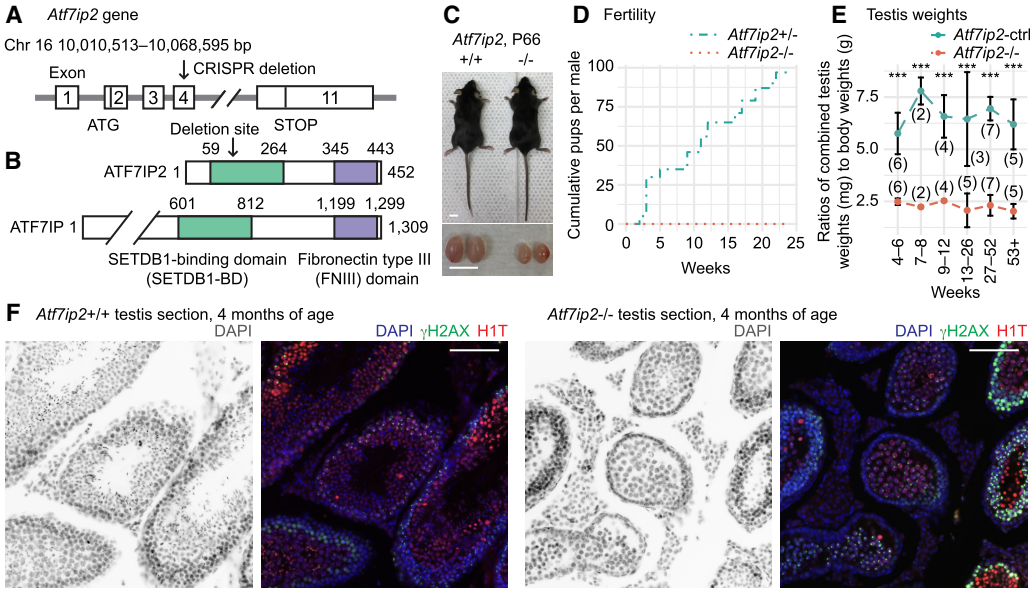

Figure 2. ATF7IP2 is required for male fertility. (*A*) Schematic of the mouse *Atf7ip2* gene and the location of the CRISPR-mediated deletion. (*B*) Schematic of mouse ATF7IP2 and ATF7IP proteins and their functional domains. (*C*) *Atf7ip2*$^{+/+}$ and *Atf7ip2*$^{-/-}$ males and their testes at postnatal day 66 (P66). Scale bars, 10 mm. (*D*) Cumulative numbers of pups sired by *Atf7ip2*$^{+/-}$ and *Atf7ip2*$^{-/-}$ males. (*E*) Testis weights for *Atf7ip2*$^{-/-}$ males and littermate controls (*Atf7ip2*-ctrl: *Atf7ip2*$^{+/+}$ and *Atf7ip2*$^{+/-}$). Numbers of independent mice analyzed are shown in parentheses. (***) $P < 0.001$, from pairwise *t*-tests adjusted with Benjamini–Hochberg post-hoc tests. Data are presented as mean ± SD. (*F*) Testis sections from *Atf7ip2*$^{+/+}$ and *Atf7ip2*$^{-/-}$ mice at 4 mo of age stained with DAPI and antibodies raised against ATF7IP2, γH2AX (a marker of the DNA damage response), and H1T (a marker of germ cells in mid-pachytene and subsequent stages). Scale bars, 100 μm.

testes compared with littermate controls (Fig. 2C–E). We confirmed the depletion of ATF7IP2 proteins in *Atf7ip2*$^{-/-}$ spermatocytes via immunofluorescence microscopy (Supplemental Fig. S2). Analyses of testicular tissue sections showed that *Atf7ip2*$^{-/-}$ testes were devoid of haploid spermatids, and seminiferous tubules were smaller than in control testes (Fig. 2F). However, *Atf7ip2*$^{-/-}$ spermatocytes reached the stage when H1T is enriched, the mid-pachytene stage, indicating that *Atf7ip2*$^{-/-}$ spermatocytes are arrested and eliminated in meiotic prophase I. Unlike *Atf7ip2*$^{-/-}$ males, *Atf7ip2*$^{-/-}$ female mice were fertile and, when crossed with *Atf7ip2*$^{+/-}$ males, gave birth at Mendelian ratios (Supplemental Fig. S3). These results suggest that the *Atf7ip2*$^{-/-}$ phenotype is caused by an essential, male-specific event in the germline that has become defective.

Meiotic phenotypes in male Atf7ip2$^{-/-}$ *mice*

To determine the function of ATF7IP2, we characterized the meiotic phenotype of *Atf7ip2*$^{-/-}$ male mice in detail. We performed immunostaining to analyze chromosome spreads from *Atf7ip2*$^{-/-}$ testes for a specific marker of the DDR: phosphorylated serine 139 of the histone variant H2AX (γH2AX). In the leptotene and zygotene stages, the DDR/checkpoint kinase ataxia telangiectasia mutated (ATM) triggers the formation of γH2AX domains throughout nuclei in response to programmed double-stranded breaks (DSBs; induced by the topoisomerase-related enzyme SPO11); with the completion of DNA repair and concomitant autosomal synapsis, γH2AX disappears from autosomes (Mahadevaiah et al. 2001; Bellani et al. 2005). In the latter steps of this process, ataxia telangiectasia and Rad3-related (ATR), another DDR/checkpoint kinase, mediates γH2AX formation on unsynapsed chromatin; in normal pachytene nuclei, this results in the confinement of γH2AX to the unsynapsed XY chromosomes, an essential event in the initiation of MSCI (Royo et al. 2013). Thus, γH2AX staining, together with SYCP3 staining, provides key insights into general meiotic phenotypes (Abe et al. 2018; Alavattam et al. 2018). In *Atf7ip2*$^{-/-}$ spermatocytes, pan-nuclear γH2AX formation occurs normally in the early/mid-zygotene stage (Fig. 3A), and relative populations of zygotene spermatocytes are comparable between *Atf7ip2*$^{-/-}$ testes and littermate controls (Fig. 3B). In the *Atf7ip2*$^{-/-}$ pachytene spermatocytes, γH2AX formation on the XY chromosomes takes place (Fig. 3A); however, we noted an increase in the relative population of early/mid-pachytene spermatocytes, whereas late pachytene and diplotene spermatocytes were rare and largely depleted from *Atf7ip2*$^{-/-}$ testes (Fig. 3B). These analyses suggest that ATF7IP2 has a critical function as spermatocytes transition from the pachytene to diplotene stages.

Following our established criteria for SYCP3- and γH2AX-based meiotic staging (Abe et al. 2018; Alavattam et al. 2018), we analyzed γH2AX staining patterns in more detail. In *Atf7ip2*$^{-/-}$ early/mid-pachytene spermatocytes, the removal of γH2AX from autosomes was disrupted in comparison with controls (Fig. 3C). In normal meiosis,

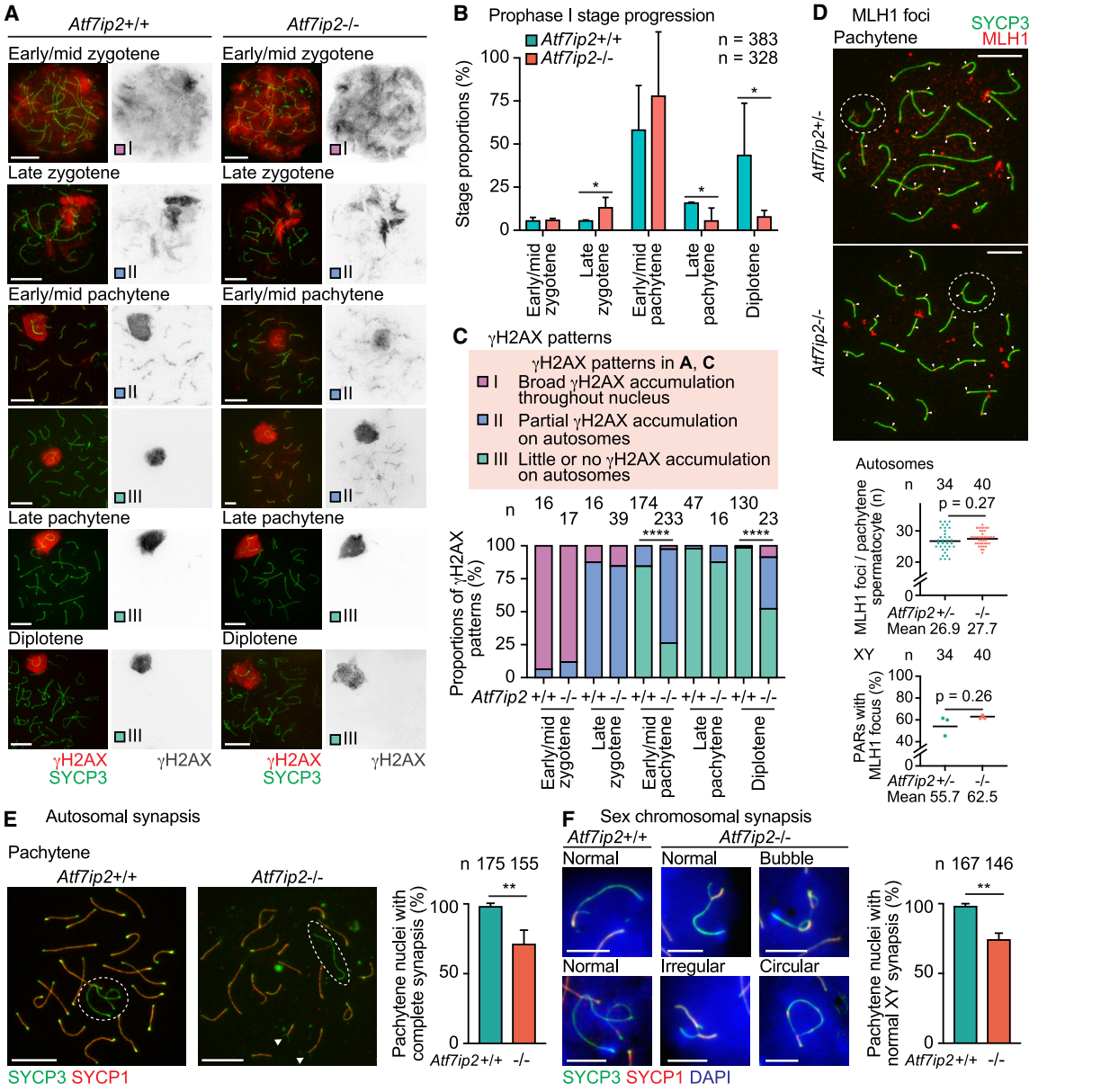

Figure 3. DDR and chromosome synapsis are mildly impaired in *Atf7ip2*$^{-/-}$ spermatocytes. (*A*) *Atf7ip2*$^{+/+}$ and *Atf7ip2*$^{-/-}$ spermatocyte chromosome spreads stained with antibodies raised against SYCP3 and γH2AX. γH2AX accumulation patterns are one of three classifications described in *C*. Scale bars, 10 µm. (*B*) Meiotic prophase I stage populations quantified as mean ± SD. Numbers of analyzed nuclei are indicated. Data are from three independent littermate pairs at P44, P66, and P69. (*) $P < 0.05$, from unpaired two-tailed *t*-tests. (*C*) Stage-wise proportions of γH2AX accumulation patterns for three independent littermate pairs and are quantified as mean ± SD. Patterns are classified with three criteria (see *top*). (****) $P < 0.0001$, from Fisher's exact tests. (*D*) Chromosome spreads stained with antibodies raised against SYCP3 and MLH1. Arrowheads indicate MLH1 foci. The *top* dot plot shows distributions of MLH1 counts. The *bottom* dot plot shows proportions of MLH1 focus-associated XY pseudoautosomal regions (PARS). Numbers of analyzed nuclei are indicated. Data are from three independent littermate pairs at P108, P115, and P122. Bars represent means. *P*-values are from unpaired *t*-tests. (*E*,*F*) Chromosome spreads stained with antibodies raised against SYCP3 (a marker of all chromosome axes) and SYCP1 (a marker of only synapsed axes). Scale bars: *E*, 10 µm; *F*, 5 µm. Bar plots show proportions of pachytene nuclei with normal synapsis of autosomes (*E*) and sex chromosomes (*F*). Data are from three independent littermate pairs at P44, P66, and P69 and are presented as mean ± SD. Numbers of analyzed nuclei are indicated. (**) $P < 0.01$, from unpaired *t*-tests.

γH2AX accumulates through the whole of leptotene and early zygotene nuclei (pattern I) (Fig. 3A,C). As spermatocytes progress into the late zygotene stage, γH2AX accumulation transitions from a pan-nuclear diffuse signal to concentrated accumulation on the chromatin associated with unsynapsed chromosome axes, albeit with partial signals remaining along synapsed autosomes (pattern II). By the mid and late pachytene stages, γH2AX is confined

to XY chromatin, having largely disappeared from autosomes (pattern III). In *Atf7ip2*$^{-/-}$ early/mid-pachytene spermatocytes, γH2AX remains on autosomes in comparison with littermate controls (Fig. 3C), suggesting that in the absence of ATF7IP2, autosomal DDR signaling is affected.

Following on this, we investigated the outcome of meiotic recombination by scoring the numbers of MLH1 foci (which illuminate crossover sites) on chromosome axes. Numbers of MLH1 foci on autosomes were comparable between *Atf7ip2*$^{+/-}$ and *Atf7ip2*$^{-/-}$ H1T-positive mid/late pachytene spermatocytes (Fig. 3D). Although a recent study of a separate *Atf7ip2*$^{-/-}$ mouse line reported reduced numbers of XY pseudoautosomal regions (PARs) with MLH1 foci (Shao et al. 2023), our observations showed no significant difference in the proportions of MLH1-associated PARs in *Atf7ip2*$^{+/-}$ and *Atf7ip2*$^{-/-}$ models (Fig. 3D). Next, we analyzed chromosome synapsis by immunostaining for SYCP3 (a marker of both unsynapsed and synapsed axes) and SYCP1 (a marker of only synapsed axes). We observed occasional but significant autosomal asynapsis in *Atf7ip2*$^{-/-}$ pachytene spermatocytes; ∼67% of *Atf7ip2*$^{-/-}$ pachytene nuclei evidenced complete synapsis, while nearly all *Atf7ip2*$^{+/+}$ spermatocytes showed complete synapsis (Fig. 3E). On occasion, the shapes of sex chromosome axes exhibited abnormal configurations, including apparent looped synapsis ("bubbles"), synapsis with large portions of itself ("irregular"), and synapsis at ends ("circular") (Fig. 3F); ∼26% of *Atf7ip2*$^{-/-}$ pachytene nuclei demonstrated abnormal sex chromosome synapsis (Fig. 3F). These results suggest that although ATF7IP2 may not play an outsized role in meiotic recombination, both DDR signaling and chromosome synapsis are impaired to some extent in *Atf7ip2*$^{-/-}$ spermatocytes.

ATF7IP2 directs SETDB1 and H3K9 methylation in male meiosis

Because ATF7IP binds SETDB1 to regulate H3K9me3 in somatic cells (Ichimura et al. 2005), we suspected that ATF7IP2 regulates H3K9me3 during meiosis. In meiotic prophase I, H3K9me3 accumulates on autosomal PCH and the sex chromosomes, where it is subject to dynamic regulation as XY undergoes MSCI (van der Heijden et al. 2007); H3K9me3 on the sex chromosomes is established by the methyltransferase SETDB1 (Hirota et al. 2018; Abe et al. 2022). Consistent with this, we observed normal H3K9me3 accumulation on autosomal PCH and XY chromatin in wild-type pachytene nuclei (Fig. 4A). Through careful examination, we noted multiple H3K9me3 accumulation patterns on the sex chromosome in the early pachytene stage of wild-type spermatocytes and recognized four general patterns: class I, covering the entirety of XY; class II, covering the entirety of Y and X-PCH; class III, covering X-PCH only; and class IV, in which H3K9me3 is absent from XY (i.e., no signal) (Fig. 4A,B; Supplemental Fig. S4A). We evaluated the proportions of patterns and found that H3K9me3 enrichment on the XY domain was impaired in the early pachytene stage of *Atf7ip2*$^{-/-}$ spermatocytes; 21% of nuclei showed essentially no signal anywhere on the XY chromosomes (class IV), a pattern that was not observed in any *Atf7ip2*$^{+/+}$ early pachytene nuclei (Fig. 4A,B). In normal mid and late pachytene stages, H3K9me3 is retained on X-PCH as it disappears from the remainder of XY chromatin (Fig. 4A), presumably due to histone replacement and the incorporation of histone variant H3.3 (van der Heijden et al. 2007). Next, in the normal diplotene stage, H3K9me3 signals promulgate through the XY chromatin in a likely reflection of H3K9me3's de novo deposition on H3.3 (Fig. 4A). However, in *Atf7ip2*$^{-/-}$ mid and late pachytene spermatocytes, H3K9me3 on X-PCH decreased, and re-establishment through the entirety of XY did not take place in the diplotene stage (Fig. 4A,C). Alongside the diplotene re-establishment of H3K9me3, H3K9me2 also accumulates on XY chromatin; however, in *Atf7ip2*$^{-/-}$ diplotene spermatocytes, we noted a clear loss of H3K9me2 (Fig. 4D,E). Concomitant with these changes, in *Atf7ip2*$^{-/-}$ spermatocytes, we observed the strong accumulation of H3K9 acetylation (H3K9ac), which counteracts H3K9 methylation, on X-PCH (Supplemental Fig. S4B). On the other hand, proportions of H3K9me1 accumulation patterns were unchanged between control and *Atf7ip2*$^{-/-}$ spermatocytes (Supplemental Fig. S4C,D), highlighting a specific role for ATF7IP2 in the regulation of H3K9me2/3 and H3K9ac. Together, these results indicate that ATF7IP2 regulates the establishment of H3K9me2/3 on diplotene XY chromatin, consistent with the concurrent, dynamic localization of ATF7IP2 from X-PCH through XY chromatin.

Given this, we hypothesized that ATF7IP2 regulates the spatiotemporal recruitment of SETDB1 (which mediates H3K9me3) to the sex chromosomes. In wild-type early and mid-pachytene nuclei, SETDB1 localizes on the XY chromosomes and is notably enriched on the X-PCH. In corresponding *Atf7ip2*$^{-/-}$ spermatocytes, SETDB1 was not enriched on X-PCH, localizing instead to sex chromosome-adjacent nucleoli (Fig. 4F). Consistent with this, *Atf7ip2*$^{-/-}$ X-PCH was less DAPI-intense compared with controls (Supplemental Fig. S5), suggesting a defect in heterochromatin formation. We also noticed that the pachytene accumulation of SETDB1 on autosomal PCH was disrupted in corresponding *Atf7ip2*$^{-/-}$ spermatocytes. In contrast to the constrained, intense SETDB1 signals of wild-type samples, we observed diffuse SETDB1 signals through the whole of mutant nuclei (Fig. 4F). We also observed that in *Setdb1* conditionally deleted mutants driven by the germline-specific *Ddx4*-Cre (*Setdb1*-cKO) (Abe et al. 2022), the accumulation of ATF7IP2 on X-PCH was significantly reduced (Supplemental Fig. S6A). Taken together, these results indicate a pan-nuclear role for ATF7IP2 in the spatiotemporal regulation of SETDB1; furthermore, at X-PCH, ATF7IP2 and SETDB1 likely operate in tandem, possibly as a protein complex.

A hallmark of normal MSCI is the sex chromosome-wide accumulation of γH2AX, and γH2AX domain formation is tightly associated with the initiation and maintenance of MSCI (Fernandez-Capetillo et al. 2003; Abe et al. 2022). γH2AX domain formation is directed by MDC1, a γH2AX-binding protein and central mediator

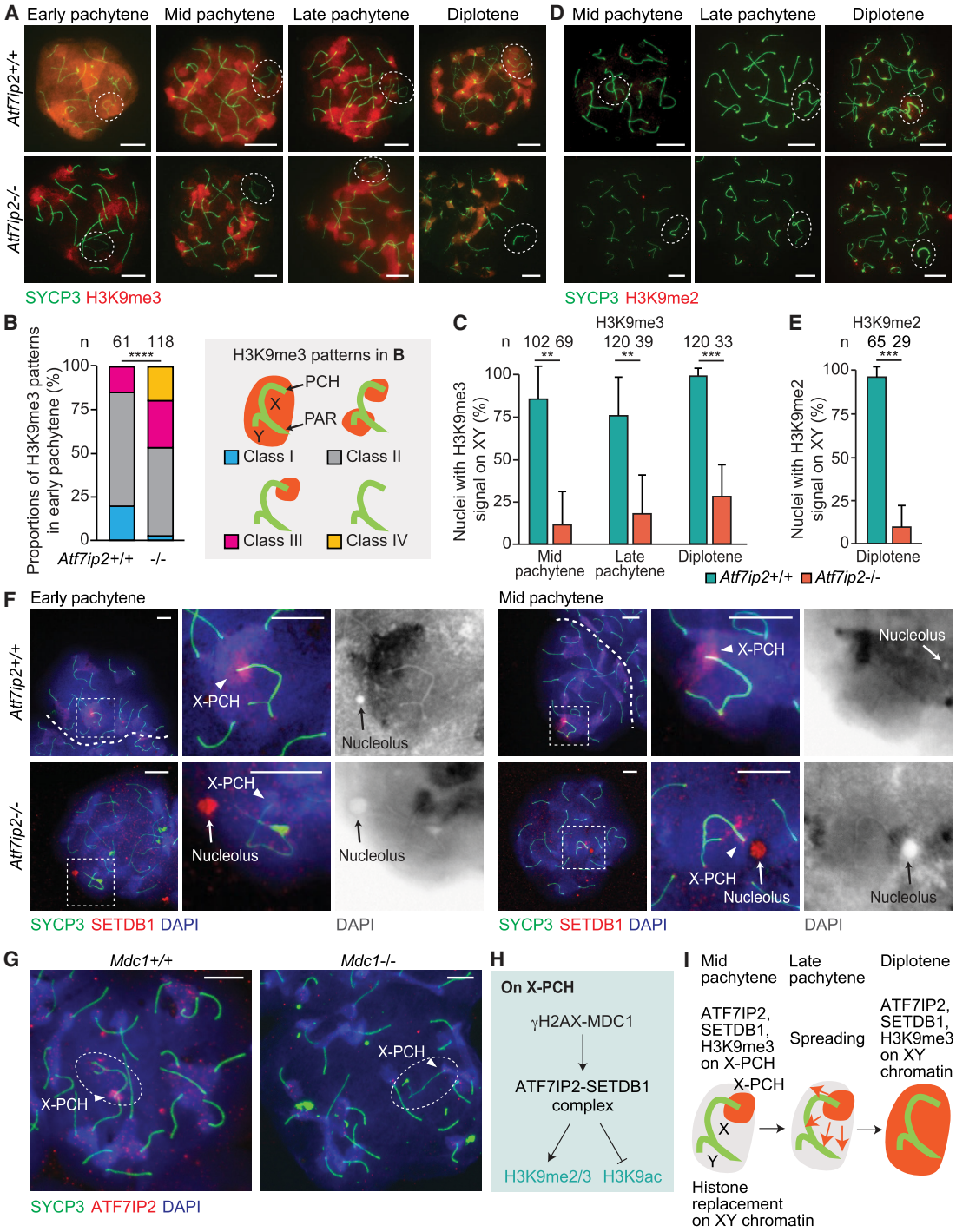

Figure 4. ATF7IP2 is required for H3K9 methylation on the sex chromosomes during male meiosis. (*A*) *Atf7ip2*$^{+/+}$ and *Atf7ip2*$^{-/-}$ spermatocyte chromosome spreads stained with antibodies raised against H3K9me3 and SYCP3 (a marker of chromosome axes, both synapsed and unsynapsed). Dashed circles indicate the sex chromosomes. Scale bars, 10 µm. (*B*) H3K9me3 accumulation patterns on the sex chromosomes of *Atf7ip2*$^{+/+}$ and *Atf7ip2*$^{-/-}$ early pachytene spermatocytes. Patterns are classified with four criteria (shown at the *right*). Data are from five independent littermate pairs and are quantified as mean ± SD. Numbers of analyzed nuclei are indicated. (****) $P < 0.0001$, from a Fisher's exact test. (*C*) Quantification of mid-pachytene, late pachytene, and diplotene spermatocytes with H3K9me3 signals on the sex chromosomes. Data are from four, six, and four independent littermate pairs, respectively, and are quantified as mean ± SD. Numbers of analyzed nuclei are indicated. (**) $P < 0.01$, (***) $P < 0.001$, from unpaired *t*-tests. (*D*) *Atf7ip2*$^{+/+}$ and *Atf7ip2*$^{-/-}$ chromosome spreads stained with antibodies raised against H3K9me2 and SYCP3. Scale bars, 10 µm. (*E*) Quantification of diplotene spermatocytes with H3K9me2 signals on the sex chromosomes for four independent experiments quantified as mean ± SD. Numbers of analyzed nuclei are indicated. (***) $P < 0.001$, from unpaired *t*-tests. (*F*) *Atf7ip2*$^{+/+}$ and *Atf7ip2*$^{-/-}$ chromosome spreads stained with antibodies raised against SETDB1 and SYCP3. Dashed squares are magnified in the panels at the *right*. Scale bars, 5 µm. (*G*) *Mdc1*$^{+/+}$ and *Mdc1*$^{-/-}$ spermatocyte chromosome spreads stained with antibodies raised against ATF7IP2 and SYCP3. Scale bars, 10 µm. (*H*) Summary of the γH2AX/MDC1–ATF7IP2–SETDB1 pathway on X-PCH. (*I*) Schematic showing the establishment of H3K9me3 on the sex chromosomes in normal mid-pachytene to diplotene spermatocytes.

of the DDR, through a feed-forward mechanism (Ichijima et al. 2011). We hypothesized that the accumulation of ATF7IP2 on XY chromatin occurs downstream from MDC1. To test this, we stained for ATF7IP2 in *Mdc1*$^{-/-}$ spermatocytes and found that in the absence of MDC1, ATF7IP2 failed to concentrate on X-PCH (Fig. 4G). Similarly, the accumulation of SETDB1 on X-PCH depended on MDC1 (Supplemental Fig. S6B). These results suggest that the MDC1-dependent DDR pathway regulates ATF7IP2 and SETDB1 localization on the sex chromosomes. We infer that, in pachytene spermatocytes, the MDC1-dependent DDR pathway recruits ATF7IP2 (presumably forming a complex with SETDB1) to X-PCH; in the subsequent diplotene stage, both factors spread through the XY chromatin, and as this occurs, SETDB1 deposits pan-XY H3K9me2/3 (Fig. 4H,I). Corroborating this model, we found that MDC1 accumulation on XY chromatin occurred independently of ATF7IP2 or SETDB1 (Supplemental Fig. S6C,D).

To parse mechanisms related to ATF7IP2, we tested the localization of related factors. A previous study suggested a role for the SETDB1-interacting protein TRIM28 as a linker between the DDR pathway and SETDB1 (Hirota et al. 2018). However, we found that TRIM28 does not localize on the sex chromosomes in wild-type meiosis (Supplemental Fig. S7A), which raises the possibility that ATF7IP2 works independently of TRIM28 to link the DDR pathway and SETDB1. In line with this possibility, TRIM28 is dispensable for male meiotic progression (Tan et al. 2020). Downstream from the DDR pathway, the chromatin remodeler CHD4 is recruited to X-PCH (Broering et al. 2014); in *Atf7ip2*$^{-/-}$ spermatocytes, CHD4 accumulation on X-PCH was unchanged from controls (Supplemental Fig. S7B). The germline-specific Polycomb protein SCML2 also accumulates in pachytene and diplotene nuclei; in *Atf7ip2*$^{-/-}$ spermatocytes, SCML2 localization did not differ from controls (Supplemental Fig. S7C,D). These results suggest that the disfunction of ATF7IP2 is not related to the localization of TRIM28, CHD4, and SCML2.

We also examined the localization of ATF7IP in *Atf7ip2*$^{-/-}$ spermatogenesis. In wild-type tissue sections, ATF7IP was predominantly found in the nuclei of primary spermatocytes (Supplemental Fig. S7E); more specifically, it localized to the X-PCH in wild-type pachytene spermatocytes (Supplemental Fig. S7F,G). Contrastingly, in *Atf7ip2*$^{-/-}$ pachytene spermatocytes, ATF7IP was absent from the X-PCH and instead localized to the XY PAR. These results demonstrate that ATF7IP2 is essential for directing ATF7IP and SETDB1 to X-PCH in pachytene spermatocytes.

ATF7IP2 is required for meiotic gene regulation

Having established its meiotic phenotype and essential role in H3K9 methylation, we sought to investigate the function of ATF7IP2 in meiotic gene regulation. To this end, we performed single-cell RNA sequencing (scRNA-seq) analyses of whole testicular cells from *Atf7ip2*$^{-/-}$ mice and their *Atf7ip2*$^{+/+}$ littermates at P15. The cellular composition of the testis changes as development progresses, leading us to confirm that in P15 testes, the first wave of spermatogenesis exhibited a similar cellular composition between *Atf7ip2*$^{+/+}$ and *Atf7ip2*$^{-/-}$ mice. Indeed, we observed this was the case until the mid to late pachytene stages, when defects appeared based on immunostaining against major markers of spermatogenesis, including ZBTB16/PLZF, STRA8, SYCP3, γH2AX, and H1T (Supplemental Fig. S8).

Using the scRNA-seq data, we endeavored to determine when ATF7IP2 functions in wild-type spermatogenesis. Since ATF7IP2 expression was restricted to germ cells, scRNA-seq data derived from germ cell populations (spermatogonia and spermatocytes) were analyzed apart from those of testicular somatic cells (Sertoli cells, Leydig cells, peritubular myoid cells, endothelial cells, and hemocytes) (Fig. 5A; Supplemental Fig. S9A,B). Using the UMAP of scRNA-seq data from *Atf7ip2*$^{+/+}$ and *Atf7ip2*$^{-/-}$ germ cell populations, we identified 13 cell type clusters; the cluster numbers are based on the numbers of cells comprising each cluster; cluster 0 is the largest, and cluster 12 is the smallest (Fig. 5B,C; Supplemental Fig. S9C,D). Assessing the expression of key marker genes for spermatogenesis with respect to the UMAP, we inferred the developmental trajectory of P15 spermatogenesis (Fig. 5D). As suggested by the high expression of *Gfra1*, cluster 8 represented a population of undifferentiated spermatogonia, including spermatogonial stem cells. Cluster 1 represented a population of differentiating spermatogonia, as indicated by the initial up-regulation of *Stra8*. Clusters 6 and 7 represented cells at the initiation of meiosis, consistent with the up-regulation of *Meiosin* and *Stra8*. Cluster 11 represented a population of spermatocytes in early meiotic prophase, as denoted by the up-regulation of *Prdm9*. Based on the expression of marker genes with respect to the UMAP, we inferred that spermatogenesis progressed along the trajectory from cluster 8 to cluster 12. Although *Atf7ip2* was expressed in a broad range of spermatogenic stages, its expression level was higher in clusters 7, 6, 11, and 5, all of which correspond to meiotic prophase (Fig. 5E). Given that *Atf7ip2* is bound by MEIOSIN and STRA8 (Fig. 1B), it is possible that the expression of *Atf7ip2* is boosted, rather than initiated, at the entry to meiosis. In contrast, *Atf7ip* is constitutively expressed in spermatogenesis (Fig. 5E).

Next, we sought to understand when cell death takes place in *Atf7ip2*$^{-/-}$ spermatocytes. Starting from cluster 8 through to cluster 5, the gene expression profiles for *Atf7ip2*$^{+/+}$ and *Atf7ip2*$^{-/-}$ germ cell populations overlapped one another to a high degree (Fig. 5A,B), indicating that *Atf7ip2*$^{-/-}$ spermatogenesis progressed until the stage of spermatogenesis that corresponds to cluster 5. However, we noticed certain subpopulations—clusters 10, 0, 2, and 3, representing B spermatogonia through to preleptotene cells—were more numerous in *Atf7ip2*$^{-/-}$ germ cells (Fig. 5C); the increased cluster sizes suggest that in the absence of ATF7IP2, the entry into meiosis is hampered. Furthermore, the subpopulation represented by cluster 12 was present in *Atf7ip2*$^{+/+}$ germ cells but missing amid *Atf7ip2*$^{-/-}$ germ cells (Fig. 5B,C).

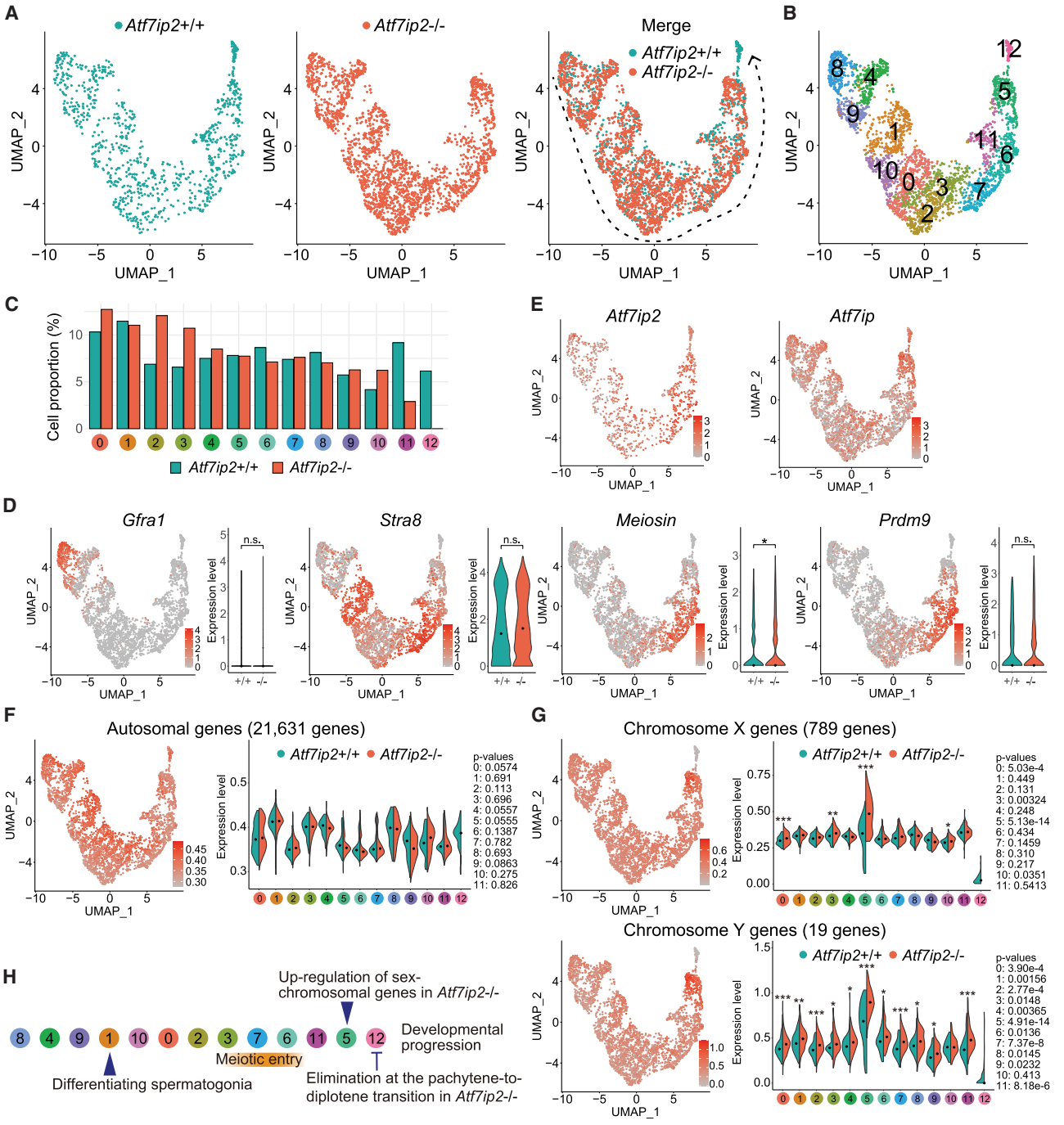

Figure 5. scRNA-seq analyses of *Atf7ip2*$^{+/+}$ and *Atf7ip2*$^{-/-}$ spermatogenic germ cells. (*A*) UMAP representations of scRNA-seq transcriptome profiles for germ cells from *Atf7ip2*$^{+/+}$ testes (*left*, P15), *Atf7ip2*$^{-/-}$ testes (*middle*, P15), and both *Atf7ip2*$^{+/+}$ and *Atf7ip2*$^{-/-}$ testes (*right*). (Gray arrow) Inferred developmental trajectory. (*B*) Clustering of UMAP-projected scRNA-seq transcriptome profiles for *Atf7ip2*$^{+/+}$ and *Atf7ip2*$^{-/-}$ germ cells based on gene expression patterns. (*C*) Bar graph showing the proportions of *Atf7ip2*$^{+/+}$ and *Atf7ip2*$^{-/-}$ germ cells among the clusters. (*D*) UMAP representations showing expression patterns for key developmental marker genes in spermatogenic cells. Genes shown include *Gfra1*, which represents undifferentiated spermatogonia; *Stra8*, which represents differentiating spermatogonia; *Meiosin*, which represents preleptotene spermatocytes; and *Prdm9*, which represents early meiotic prophase spermatocytes. (n.s.) Not significant, (*) $P < 0.05$, from Wilcoxon rank sum tests. (*E*) Expression patterns for *Atf7ip2* and *Atf7ip* upon the UMAP. (*F*) Expression levels for autosomal genes. (*G*) Expression levels for X-chromosomal genes (*top*) and Y-chromosomal genes (*bottom*) are shown. (*) $P < 0.05$, (**) $P < 0.01$, (***) $P < 0.001$, from Wilcoxon rank sum tests. (*H*) Summary of *Atf7ip2*$^{-/-}$ phenotypes in spermatogenic germ cells. Subtype clusters are ordered by inferred developmental progression. Key cell types and events in *Atf7ip2*$^{+/+}$ and *Atf7ip2*$^{-/-}$ spermatogenesis are shown.

Furthermore, in *Atf7ip2*$^{+/+}$ germ cells, expression levels of sex-linked genes were abruptly down-regulated in the transition from cluster 5 to cluster 12 compared with that of autosomal genes (Fig. 5F,G). Intriguingly, in *Atf7ip2*$^{-/-}$ cells, cluster 5 was associated with a strong, abrupt up-regulation of sex-linked gene expression (Fig. 5G), suggesting that MSCI failure began in the cluster 5 subpopulation of *Atf7ip2*$^{-/-}$ cells. Thus, the loss of the cluster 12 subpopulation in *Atf7ip2*$^{-/-}$ testes was preceded by an ectopic up-regulation of X- and Y-chromosomal genes in cluster 5 (Fig. 5G), indicating that clusters 5 and 12 represent pachytene spermatocytes.

Remarkably, gene enrichment analysis revealed that genes related to late spermatogenesis (e.g., *Clgn*, *Hspa2*, *Piwil1*, and *Ldhc*) were highly expressed in the cluster 12 subpopulation of spermatocytes (Supplemental Fig. S9C; Supplemental Table S1). Because those genes are known to be expressed in the late pachytene stage onward, we inferred that cluster 12 corresponds to cytologically defined late pachytene spermatocytes (and/or diplotene spermatocytes). It is important to note that aligning exact substages between cytology-defined and gene expression-based criteria can be challenging. However, the single-cell RNA sequencing (scRNA-seq) results aligned well with cytological observations, indicating that *Atf7ip2*$^{-/-}$ spermatocytes progress through early meiotic prophase but are predominantly eliminated via cell death during the transition from the late pachytene to diplotene stages (Fig. 3B). Thus, ATF7IP2 is required for spermatocytes to progress beyond the pachytene-to-diplotene transition (Fig. 5H).

ATF7IP2 binds broadly to the sex chromosomes and autosomal gene promoters

To determine where ATF7IP2 binds the genome of wild-type pachytene spermatocytes, we performed CUT&Tag for ATF7IP2 in two biological replicates. We observed the specific enrichment of ATF7IP2 CUT&Tag signals relative to IgG CUT&Tag signals (Supplemental Fig. S10A). Given the high correlation between replicates (Supplemental Fig. S10B), we combined them for subsequent analyses. Analyses of ATF7IP2 coverage revealed 61,839 genome-wide regions of enriched ATF7IP2 binding; i.e., "ATF7IP2 peaks" (Fig. 6A). We observed ATF7IP2 peaks on TSSs (26.73%), gene bodies (27.74%), TESs (0.1%), and intergenic regions (45.43%). TSS peaks were enriched on autosomes, whereas intergenic peaks were enriched on the sex chromosomes (Fig. 6A), suggesting distinct functions for ATF7IP2 on the autosomes and sex chromosomes. In our continued investigation of wild-type pachytene spermatocytes, we conducted a clustering analysis incorporating ATF7IP2 peaks, regions of H3K9me3 coverage (data newly generated for this study, shown in Supplemental Fig. S10C), and regions of coverage for the active promoter mark H3K4me3 (data from our previous study, as shown in Maezawa et al. 2018b); this analysis resulted in three distinct clusters (Fig. 6B). Cluster I regions (6632) are associated with H3K4me3 deposition (Fig. 6B) on autosomes and at TSSs (Fig. 6C,D). Cluster II regions (22,579) are associated with broad H3K9me3 enrichment (Fig. 6B); 70% of these regions are on the sex chromosomes (Fig. 6C), mostly at intergenic regions and gene bodies (Fig. 6D), which is in line with the role of ATF7IP2 in the regulation of H3K9me3 on the sex chromosomes. Cluster III regions (32,628) largely represent autosomal intergenic regions and gene bodies (Fig. 6C,D).

Based on the enrichment of ATF7IP2 at TSSs, we sought to identify ATF7IP2 target genes in pachytene spermatocytes. Our analyses revealed 4917 autosomal genes and 270 sex chromosomal genes (Supplemental Table S2). ATF7IP2 binds the promoters of a broad range of genes required for meiotic prophase and spermiogenesis, including *Hormad1* and *Sycp3*, both autosomal genes, as well

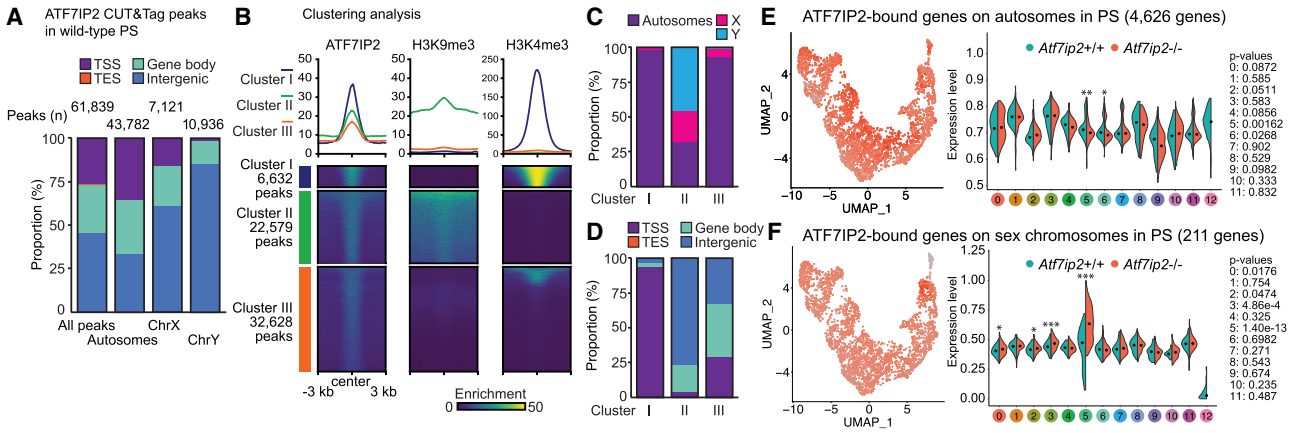

Figure 6. ATF7IP2-binding sites in pachytene spermatocytes. (*A*) Numbers and genomic distribution of ATF7IP2 CUT&Tag peaks in wild-type pachytene spermatocytes. (*B*) Clustering analysis of ATF7IP2 CUT&Tag peaks and H3K9me3- and H3K4me3-enriched regions. Average tag density profiles (*top*) and heat maps (*bottom*) for each cluster are shown. (*C*) Chromosomal distribution of ATF7IP2 peak clusters. (*D*) Genomic distribution of ATF7IP2 peak clusters. (*E*) Expression levels of ATF7IP2-bound autosomal genes in scRNA-seq. (*) $P < 0.05$, (**) $P < 0.01$, from Wilcoxon rank sum tests. (*F*) Expression levels for ATF7IP2-bound sex chromosomal genes in scRNA-seq. (*) $P < 0.05$, (***) $P < 0.001$, from Wilcoxon rank sum tests.

as Y-linked *Zfy1*. These promoter peaks are associated with the active histone modifications H3K4me3 and H3K27ac (Supplemental Fig. S10D). Next, using our scRNA-seq data set for *Atf7ip2*$^{+/+}$ and *Atf7ip2*$^{-/-}$ spermatogenic germ cells, we sought to understand the regulation of ATF7IP2 target genes. We detected the expression of 4626 ATF7IP2 target genes on autosomes and 211 ATF7IP2 target genes on the sex chromosomes. The autosomal genes were down-regulated in *Atf7ip2*$^{-/-}$ pachytene spermatocytes (Fig. 6E, clusters 6 to 5, representing the early to mid-pachytene stages). Because wild-type autosomal promoter peaks are associated with H3K4me3, these results indicate that ATF7IP2 binds to and positively regulates the expression of these genes. On the other hand, in *Atf7ip2*$^{-/-}$ pachytene spermatocytes, the 211 sex chromosomal genes are highly up-regulated in cluster 5 (Fig. 6F, mid-pachytene spermatocytes), indicating that ATF7IP2 binds to and negatively regulates the expression of these genes. These results reveal two separate functions for ATF7IP2 in pachytene spermatocytes: one for autosomal gene expression and, contrastingly, another for sex chromosomal gene repression.

ATF7IP2 directs meiotic gene regulation

To elucidate gene regulatory mechanisms associated with ATF7IP2, we isolated pachytene spermatocytes from both *Atf7ip2*$^{+/+}$ and *Atf7ip2*$^{-/-}$ testes and, after confirming their purity, conducted bulk RNA sequencing with ERCC spike-in controls across three biological replicates. The transcription data derived from this process were then analyzed (Supplemental Fig. S10E,F; Supplemental Table S3). While isolating the cells, we were surprised to observe that *Atf7ip2*$^{-/-}$ spermatocytes were smaller than their *Atf7ip2*$^{+/+}$ counterparts (Supplemental Fig. S10E). This gross decrease in size suggests that in *Atf7ip2*$^{-/-}$ spermatocytes, the pachytene transcriptional burst (Maezawa et al. 2020) is compromised, a possibility consistent with the global down-regulation of ATF7IP2-bound autosomal genes detected with scRNA-seq.

Comparing the spike-in-normalized mutant and control RNA-seq data, we identified 9446 autosomal differentially expressed genes (DEGs)—218 up-regulated and 9228 down-regulated (Fig. 7A). To understand how autosomal DEGs are expressed during normal spermatogenesis, we reanalyzed separate RNA-seq data taken from cell types sampled across wild-type spermatogenesis (Maezawa et al. 2018b). The 218 up-regulated genes displayed high expression levels in wild-type spermatogonia but were suppressed in wild-type pachytene spermatocytes (Supplemental Fig. S11A). Thus, their up-regulation in *Atf7ip2*$^{-/-}$ pachytene spermatocytes suggests an ectopic expression of normally repressed premeiotic genes. The top gene ontology (GO) (Ashburner et al. 2000) enrichment terms for these genes are related to immune system functions (Supplemental Fig. S11B), suggesting that ATF7IP2 suppresses the expression of immune genes in pachytene spermatocytes. In contrast, many of the 9228 down-regulated genes were highly expressed in wild-type pachytene spermatocytes (Supplemental Fig. S11A), and the associated GO enrichment terms were related to spermatogenesis (Supplemental Fig. S11B). These findings indicate that many spermatogenesis-related genes fail to activate in *Atf7ip2*$^{-/-}$ pachytene spermatocytes. Furthermore, in *Atf7ip2*$^{-/-}$ spermatocytes, *Atf7ip* expression was decreased (Supplemental Fig. S11C). Shifting focus to the sex chromosomes, we detected 539 DEGs associated with the *Atf7ip2*$^{-/-}$ pachytene X chromosome; 533 were up-regulated in mutants relative to controls, whereas six were down-regulated (Fig. 7A). On the Y chromosome, 12 DEGs were up-regulated, and we detected no down-regulated DEGs (Fig. 7A). These results are largely consistent with bulk RNA-seq analyses of P14 juvenile testes (Supplemental Fig. S12), together indicating that MSCI is disrupted in *Atf7ip2*$^{-/-}$ pachytene spermatocytes.

We next examined the regulation of ATF7IP2 target genes in *Atf7ip2*$^{-/-}$ pachytene spermatocytes. A significant overlap exists between these target genes and DEGs in *Atf7ip2*$^{-/-}$ spermatocytes (Supplemental Fig. S11D). Notably, there is a considerable intersection between down-regulated autosomal DEGs and ATF7IP2 autosome targets, with an enrichment in key processes such as mRNA and DNA metabolism, as well as translation (Supplemental Fig. S11D). This indicates a direct regulatory role for ATF7IP2 in vital cellular functions. Furthermore, there is a significant overlap between XY up-regulated DEGs and ATF7IP2 XY targets (Supplemental Fig. S11E), reinforcing our conclusion that ATF7IP2 is involved in suppressing gene expression to preserve MSCI.

MSCI is initiated by the DDR pathway and maintained through active DDR signaling (Ichijima et al. 2011; Abe et al. 2022). On the *Atf7ip2*$^{-/-}$ XY domain, γH2AX signals were observed (Fig. 2), but H3K9me2/3 deposition was not established as the pachytene stage progressed into the diplotene stage (Fig. 4). Indeed, in place of H3K9me2/3, we observed signals for the active transcriptional mark H3K9ac (Supplemental Fig. S4B). Thus, we suspect that MSCI is initiated but not maintained in *Atf7ip2*$^{-/-}$ spermatocytes. To test this, we stained for POLII in *Atf7ip2*$^{-/-}$ pachytene spermatocytes. In normal mid-pachytene spermatocytes, we observed the exclusion of POLII from XY domains in 100% of observed nuclei ($n = 65$) (Supplemental Fig. S11F), confirming the accurate detection of MSCI through POLII immunostaining. However, in *Atf7ip2*$^{-/-}$ mid-pachytene spermatocytes, we observed the exclusion of POLII from XY chromatin in only 73.3% of nuclei ($n = 105$) (Supplemental Fig. S11G); 26.7% of *Atf7ip2*$^{-/-}$ nuclei included POLII in XY domains (Supplemental Fig. S11H), which is evidence for defective MSCI. These results suggest that in the absence of ATF7IP2, the initiation of MSCI occurs, but MSCI fails to be maintained.

To understand the mechanism through which ATF7IP2 regulates H3K9me3 deposition, we produced and analyzed H3K9me3 CUT&RUN data from *Atf7ip2*$^{+/+}$ and *Atf7ip2*$^{-/-}$ pachytene spermatocytes (Supplemental Fig. S10G). We found that H3K9me3 is largely dependent on ATF7IP2, especially at the sites of cluster II ATF7IP2-bound peaks (Fig. 7C; cluster II peaks are defined in Fig. 6B). ATF7IP2 and H3K9me3 signals frequently overlapped, with many regions of H3K9me3 deposition

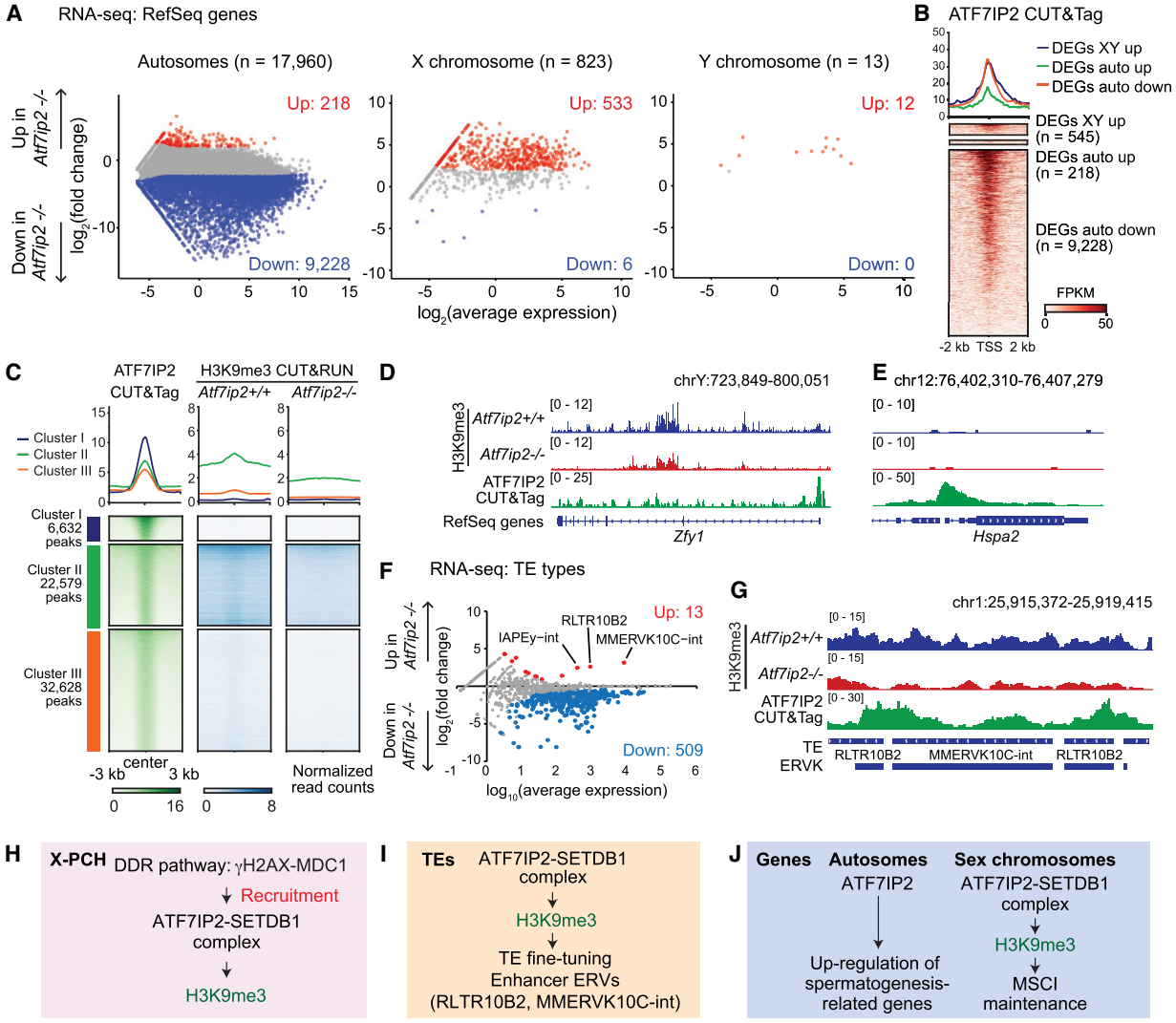

Figure 7. ATF7IP2 directs meiotic gene regulation and regulates TEs. (*A*) Comparison of *Atf7ip2*$^{+/+}$ and *Atf7ip2*$^{-/-}$ pachytene spermatocyte transcriptomes. Autosomal, X, and Y genes were analyzed separately. Three independent biological replicates were examined. All genes with adjusted *P*-values (Benjamini–Hochberg method) are plotted. Differentially expressed genes (DEGs; $\log_2$ fold change > 2, adjusted *P*-value < 0.05) are indicated by color ([red] up-regulated in *Atf7ip2*$^{-/-}$, [blue] down-regulated in *Atf7ip2*$^{-/-}$), and numbers are shown. (*B*) ATF7IP2 CUT&Tag enrichment at DEG TSSs ± 2 kb in wild-type pachytene spermatocytes. Average tag density profiles (*top*) and heat maps (*bottom*) for each cluster are shown. (*C*) ATF7IP2 CUT&Tag and H3K9me3 CUT&RUN enrichment in clusters I–III (defined in Fig. 6B). Average tag density profiles (*top*) and heat maps (*bottom*) for each cluster are shown. (*D*,*E*) Track views of the *Zfy1* locus (an up-regulated Y-linked locus) and the *Hspa2* locus (a down-regulated autosomal locus). (*F*) Comparison of *Atf7ip2*$^{+/+}$ and *Atf7ip2*$^{-/-}$ pachytene spermatocyte transposable element (TE) expression. All TE types are plotted. Differentially expressed TE types (DEGs; $\log_2$ fold change > 2, adjusted *P*-value < 0.05) are indicated by color ([red] up-regulated in *Atf7ip2*$^{-/-}$, [blue] down-regulated in *Atf7ip2*$^{-/-}$), and numbers are shown. (*G*) Track view of the ATF7IP2 targeted TEs RLTR10B2 and MMERVK10C-int. (*H*) Summary and model of the function of ATF7IP2 on X-PCH. (*I*) Summary and model of the function of ATF7IP2 in TE regulation. (*J*) Summary and model of the function of ATF7IP2 in gene expression regulation.

centered on ATF7IP2 peaks (Fig. 7C). Notably, H3K9me3 deposition was completely absent or strongly diminished in the *Atf7ip2*$^{-/-}$ model, indicating that H3K9me3 enrichment is dependent on ATF7IP2 (Fig. 7C). As shown in a track view of the Y-linked *Zfy1* locus, ATF7IP2-binding sites frequently align with, or are immediately adjacent to, locations of ATF7IP2-dependent H3K9me3 (Fig. 7D). Conversely, there was no observed H3K9me3 enrichment on ATF7IP2-dependent autosomal genes, as evidenced by loci such as *Hspa2* (Fig. 7E). We conclude that ATF7IP2 directs H3K9me3 deposition while simultaneously orchestrating meiotic gene activation on autosomes, much of which is independent of H3K9me3. Furthermore, by categorizing H3K9me3 peaks in wild-type pachytene spermatocytes based on their ATF7IP2 binding status, we revealed a reduction in H3K9me3 enrichment in both ATF7IP2-bound and unbound regions in *Atf7ip2*$^{-/-}$ spermatocytes (Supplemental Fig. S10H). This finding

supports a model in which ATF7IP2 potentially governs H3K9me3 levels by regulating the nuclear localization of SETDB1.

ATF7IP2 fine-tunes the expression of transposable elements

SETDB1-mediated H3K9me3 is a well-known suppressor of transposable elements (TEs) (Matsui et al. 2010; Rowe et al. 2013). Therefore, we sought to examine TE expression using our RNA-seq data in combination with a "best-match" TE annotation set (Sakashita et al. 2020), which enabled the detection of alignments uniquely mapped to TEs that are not exon-derived (mRNA-derived). This strategy eliminated detection of TEs that are parts of mRNA, preventing the conflation of mRNA and TE expression. In *Atf7ip2*$^{-/-}$ pachytene spermatocytes, we observed an up-regulation of 13 TE types, including IAPEy-int, RLTR10B2, and MMERVK10C-int, whereas 509 types were down-regulated (Fig. 7F; Supplemental Table S4). This up-regulation, particularly of IAPEy-int, RLTR10B2, and MMERVK10C-int, was further confirmed by scRNA-seq analysis (Supplemental Fig. S13). ATF7IP2 was found to bind these up-regulated TEs, with the H3K9me3 enrichment at these loci being dependent on ATF7IP2 (Fig. 7G). In wild-type spermatogenesis, TE expression undergoes dynamic changes at the mitosis-to-meiosis transition, and a subset of TEs—specifically, endogenous retrovirus K (ERV) families that are also known as long-terminal repeats (LTRs)—are activated as enhancers in meiosis (Sakashita et al. 2020). Notably, these meiotic enhancer ERVs (RLTR10B2) are among the up-regulated TEs (Fig. 7F). The meiotic enhancer ERVs are active in wild-type pachytene spermatocytes and are further up-regulated in *Atf7ip2*$^{-/-}$ cells. Thus, ATF7IP2 may fine-tune the activity of these TEs. In contrast, various TE types, particularly those enriched with LTRs and active in the pachytene stage, are down-regulated in *Atf7ip2*$^{-/-}$ spermatocytes. In all, our study identified distinct functions for ATF7IP2 in regulating protein-coding genes on autosomes and sex chromosomes, as well as in the regulation of TEs (Fig. 7H–J).

Discussion

Our study identified ATF7IP2 as a counterpart to ATF7IP that is highly expressed in the male germline and directs SETDB1-mediated H3K9 methylation—a conclusion supported by two major observations. First, in wild-type meiosis, ATF7IP2, SETDB1, and H3K9me3 accumulate on autosomal PCH; in pachytene spermatocytes, all are enriched on the X-PCH, the site from which they spread through the diplotene XY domain. Second, in *Atf7ip2*$^{-/-}$ pachytene spermatocytes, SETDB1 was grossly delocalized, and H3K9me2/3 was largely absent on the XY chromatin in the late pachytene to diplotene stages. As might be expected, the *Atf7ip2*$^{-/-}$ meiotic phenotype overlaps to some extent the meiotic phenotype of *Setdb1*-cKO mice. Thus, our study revealed the molecular logic for the management of SETDB1 and H3K9me3 in meiosis, demonstrating the unique nature of meiotic heterochromatin and its distinct regulation with respect to autosomes and the sex chromosomes.

However, in the early pachytene stage, there is a phenotypic difference between *Atf7ip2*$^{-/-}$ and *Setdb1*-cKO mice with regard to H3K9me3 localization: H3K9me3, a SETDB1-dependent marker of XY chromatin (Hirota et al. 2018; Abe et al. 2022), is affected by but not completely absent from XY chromatin in *Atf7ip2*$^{-/-}$ mice. Thus, there may be an alternate regulator of SETDB1 in early pachytene spermatocytes. In support of this possibility, *Setdb1*-cKO spermatocytes evidenced more severe chromosome synapsis defects (Hirota et al. 2018; Cheng et al. 2021; Abe et al. 2022) than *Atf7ip2*$^{-/-}$ spermatocytes. Nevertheless, the meiotic arrest phenotype indicates that the ATF7IP2-dependent regulation of SETDB1 (likely through an ATF7IP2–SETDB1 complex) and H3K9me3 becomes essential in the pachytene-to-diplotene transition. Curiously, we found that ATF7IP2 regulates ATF7IP localization in meiosis, highlighting the critical role of ATF7IP2 in meiosis. Although *Atf7ip* expression was reduced in the *Atf7ip2*$^{-/-}$ spermatocytes, in our ATF7IP2 CUT&Tag analysis, ATF7IP2 did not appear to bind to the *Atf7ip* gene promoter. We infer that the observed effects could be attributed to an indirect influence.

Our study also revealed novel aspects of the meiotic sex chromosomes. We propose that, through the recruitment of SETDB1, ATF7IP2 functions as an effector that links DDR signaling and SETDB1-mediated H3K9me3. The γH2AX-binding partner MDC1 is necessary for the recruitment of ATF7IP2 to X-PCH (Fig. 4G). A previous study proposed that TRIM28 (KAP1), a SETDB1 partner in ERV suppression, links the DDR and SETDB1 on the meiotic sex chromosomes (Hirota et al. 2018). However, we did not observe TRIM28 enrichment on XY, and so we question TRIM28's status as a linker. Furthermore, it was reported that young *Trim28* mutant mice are initially fertile and only become sterile with age (Tan et al. 2020), indicating that TRIM28 is not essential for MSCI.

We found that the enrichment of H3K9me2/3 on diplotene XY chromatin is largely ATF7IP2-dependent. Given the extensive histone replacement that occurs in MSCI (H3.1/H3.2 to H3.3) (van der Heijden et al. 2007), H3K9me2/3 deposition is likely to take place on "fresh" H3.3. In the latter stages of spermatogenesis, H3K9me2/3 is a persistent mark on the sex chromosomes, from MSCI to postmitotic silencing (Namekawa et al. 2007); thus, the ATF7IP2-dependent mechanisms described here could be driving heritable epigenetic states through meiotic divisions.

Unexpectedly, our study demonstrates that ATF7IP2 is required for global gene regulation in pachytene spermatocytes. In mid-pachytene spermatocytes, a burst of gene activation takes place that is driven by the transcription factor A-MYB (MYBL1) through the activation of meiotic enhancers (Bolcun-Filas et al. 2011; Maezawa et al. 2020). Thus, there is an intriguing possibility that such meiosis-specific transcription requires ATF7IP2. Importantly, ATF7IP2 is present at thousands of autosomal promoters,

where H3K9me3 is notably absent. Thus, ATF7IP2 could regulate transcriptional mechanisms independent of H3K9me3. Intriguingly, ATF7, an ATF7IP2-interacting protein, also accumulates on a wide range of autosomal promoters in testicular germ cells, mediating epigenetic inheritance through the regulation of H3K9me2 (Yoshida et al. 2020). In future studies, a key goal will be to determine the mechanistic relationship between ATF7IP2 and ATF7 in the context of meiotic gene regulation. While ATF7IP2's localization on the sex chromosomes requires MDC1, it is unknown what regulates its recruitment to autosomes, although one possibility is ATM-dependent DDR signaling. Furthermore, it is unknown what coordinates ATF7IP2's distinct autosomal and XY functions.

Finally, we show that ATF7IP2 fine-tunes the expression of retrotransposon-derived loci in male germ cells, a function that coincides with SETDB1's role in TE silencing. In *Atf7ip2*$^{-/-}$ spermatocytes, we observed the up-regulated expression of immune genes, a phenomenon akin to SETDB1-mediated immune escape in tumorigenesis (Griffin et al. 2021). In tumor cells, the depletion of SETDB1 facilitates the expression of immune genes, thereby driving the intrinsic immunogenicity of tumors. Also in tumor cells, SETDB1 works together with the HUSH complex—itself functionally linked to ATF7IP (Timms et al. 2016)—to suppress large domains of the genome enriched for rapidly evolved TEs (Griffin et al. 2021). Notably, a large number of the germline genes activated in pachytene spermatocytes are rapidly evolved (Soumillon et al. 2013), as are the meiotic ERV enhancer loci that drive germline gene expression (Sakashita et al. 2020). In wild-type spermatocytes, these loci are associated with broad domains of H3K9me3. Furthermore, like many tumor cells, testicular germ cells are immunoprivileged, found beyond the blood–testis barrier. Given the similarities between germ and tumor cells, it is possible that ATF7IP2-directed SETDB1 mechanisms, which regulate MSCI and TEs, drive the quick-paced evolution of the germline genome. It may be that this work establishes a foundation to understand the mechanisms behind germline evolution in mammals.

A recent study reported another *Atf7ip2* mutant mouse line (Shao et al. 2023), and although the mouse phenotypes detailed in the two studies were largely consistent, we did not observe the reported difference in XY obligatory crossover (Shao et al. 2023). This could be due to an *Atf7ip2* mutational difference in the mouse lines. Further investigations are warranted to clarify the role of ATF7IP2 in male meiosis.

Materials and methods

Animals

All mice were handled according to the guidelines of the Institutional Animal Care and Use Committee (IACUC; protocol nos. IACUC2018-0040 and 21931) at Cincinnati Children's Hospital Medical Center and the University of California, Davis.

Generation of Atf7ip2$^{-/-}$ *mice*

Atf7ip2$^{-/-}$ mice were generated using an sgRNA (target sequence TTCATGTCTACTCTTGCACT) that was selected according to location and the on-target and off-target scores from the web tool CRISPOR (Haeussler et al. 2016).

Preparation of meiotic chromosome spreads

Meiotic chromosome spread preparation, immunostaining, and data analysis were performed as described previously (Alavattam et al. 2018). Histology and immunostaining were performed as described previously (Abe et al. 2022).

Isolation of pachytene spermatocytes

Isolation of pachytene spermatocytes using fluorescence-activated cell sorting (FACS) was performed using an SH800S Cell Sorter (Sony), with Vybrant DyeCycle Violet (DCV)-stained (Invitrogen V35003) testicular single-cell suspensions prepared as described previously (Yeh et al. 2021).

Next-generation sequencing analysis

Library generation and data analyses for bulk RNA-seq, CUT&Tag, CUT&RUN, and scRNA-seq are described in the Supplemental Material.

Other detailed experimental procedures are described in the Supplemental Material.

Data availability

RNA-seq data and CUT&RUN/Tag data sets were deposited in the Gene Expression Omnibus (accession no. GSE244088). Bulk RNA-seq data for testes were deposited in the Gene Expression Omnibus (accession no. GSE223742). Single-cell RNA-seq data are available at the DNA Databank of Japan (DDBJ) Sequence Read Archive (DRA) under BioProject accession number PRJDB16643.

Competing interest statement

The authors declare no competing interests.

Acknowledgments

We thank Yoshinori Watanabe, Hiroki Shibuya, Akihiro Morimoto, and Shohei Yamamoto for their contributions to the early stage of this investigation; members of the Namekawa laboratory for discussion and helpful comments regarding this manuscript; So Maezawa and Masashi Yukawa for the initial RNA-seq analysis; Neil Hunter and Richard M. Schultz for discussion; Yasuhiro Fujiwara and Yuki Okada for aiding in the transfer of the anti-ATF7IP2 antibody; the Transgenic Animal and Genome Editing Core at Cincinnati Children's Hospital Medical Center for generation of the *Atf7ip2*$^{-/-}$ mouse model; Yoichi

Shinkai for providing the *Setdb1* floxed mouse line; Junjie Chen for providing the *Mdc1*-KO mice; and Mary Ann Handel for providing the anti-H1T antibody. Funding was received from National Institutes of Health (NIH) Training Program in Molecular and Cellular Biology grant T32GM007377 and a Ford Foundation Predoctoral Fellowship to J.M.E.; R01 GM134731 to P.R.A.; Grants-in-Aid for Scientific Research (KAKENHI) grants 19H05743 and 23H00379, Japan Agency for Medical Research and Development (AMED), Precursory Research for Innovative Medical Care (PRIME) grant 23gm6310021h0003, and the program of the Research for High Depth Omics, Institute of Molecular Embryology and Genetics Kumamoto University to K.-I.I.; and a University of California, Davis, startup fund and NIH R01 GM098605, R35 GM141085, and GM141085 diversity supplements to S.H.N.

Author contributions: K.G.A., J.M.E., M.H., R.S., K.-I.I., and S.H.N. designed the study. K.G.A., J.M.E., M.H., A.R.K., H.A., Y.K., Y.-H.Y., and J.K. performed experiments. K.G.A., J.M.E., M.H., A.R.K., H.A., and Y.K. analyzed the mouse phenotypes. J.M.E. and M.H. isolated germ cells and performed scRNA-seq experiments. M.H. performed bulk RNA-seq, CUT&Tag, and CUT&RUN experiments. R.S. analyzed the scRNA-seq data. K.G.A., J.M.E., M.H., R.S., Y.M., K.O., S.Y., K.-I.I., and S.H.N. designed and interpreted the computational analyses. Y.-C.H. generated the *Atf7ip2*$^{-/-}$ mouse line. K.G.A., J.M.E., M.H., R.S., P.R.A., K.-I.I., and S.H.N. interpreted the results and wrote the manuscript with critical feedback from all other authors. S.H.N. supervised the project.

References

Abe H, Alavattam KG, Kato Y, Castrillon DH, Pang Q, Andreassen PR, Namekawa SH. 2018. CHEK1 coordinates DNA damage signaling and meiotic progression in the male germline of mice. *Hum Mol Genet* **27:** 1136–1149. doi:10.1093/hmg/ddy022

Abe H, Yeh YH, Munakata Y, Ishiguro KI, Andreassen PR, Namekawa SH. 2022. Active DNA damage response signaling initiates and maintains meiotic sex chromosome inactivation. *Nat Commun* **13:** 7212. doi:10.1038/s41467-022-34295-5

Alavattam KG, Kato Y, Sin HS, Maezawa S, Kowalski IJ, Zhang F, Pang Q, Andreassen PR, Namekawa SH. 2016. Elucidation of the Fanconi anemia protein network in meiosis and its function in the regulation of histone modifications. *Cell Rep* **17:** 1141–1157. doi:10.1016/j.celrep.2016.09.073

Alavattam KG, Abe H, Sakashita A, Namekawa SH. 2018. Chromosome spread analyses of meiotic sex chromosome inactivation. *Methods Mol Biol* **1861:** 113–129. doi:10.1007/978-1-4939-8766-5_10

Alavattam KG, Maezawa S, Andreassen PR, Namekawa SH. 2022. Meiotic sex chromosome inactivation and the XY body: a phase separation hypothesis. *Cell Mol Life Sci* **79:** 18. doi:10.1007/s00018-021-04075-3

Ashburner M, Ball CA, Blake JA, Botstein D, Butler H, Cherry JM, Davis AP, Dolinski K, Dwight SS, Eppig JT, et al. 2000. Gene ontology: tool for the unification of biology. The gene ontology consortium. *Nat Genet* **25:** 25–29. doi:10.1038/75556

Becker JS, Nicetto D, Zaret KS. 2016. H3K9me3-dependent heterochromatin: barrier to cell fate changes. *Trends Genet* **32:** 29–41. doi:10.1016/j.tig.2015.11.001

Bellani MA, Romanienko PJ, Cairatti DA, Camerini-Otero RD. 2005. SPO11 is required for sex-body formation, and Spo11 heterozygosity rescues the prophase arrest of *Atm*$^{-/-}$ spermatocytes. *J Cell Sci* **118:** 3233–3245. doi:10.1242/jcs.02466

Berrios S. 2017. Nuclear architecture of mouse spermatocytes: chromosome topology, heterochromatin, and nucleolus. *Cytogenet Genome Res* **151:** 61–71. doi:10.1159/000460811

Bilodeau S, Kagey MH, Frampton GM, Rahl PB, Young RA. 2009. SetDB1 contributes to repression of genes encoding developmental regulators and maintenance of ES cell state. *Genes Dev* **23:** 2484–2489. doi:10.1101/gad.1837309

Bolcun-Filas E, Bannister LA, Barash A, Schimenti KJ, Hartford SA, Eppig JJ, Handel MA, Shen L, Schimenti JC. 2011. A-MYB (MYBL1) transcription factor is a master regulator of male meiosis. *Development* **138:** 3319–3330. doi:10.1242/dev.067645

Broering TJ, Alavattam KG, Sadreyev RI, Ichijima Y, Kato Y, Hasegawa K, Camerini-Otero RD, Lee JT, Andreassen PR, Namekawa SH. 2014. BRCA1 establishes DNA damage signaling and pericentric heterochromatin of the X chromosome in male meiosis. *J Cell Biol* **205:** 663–675. doi:10.1083/jcb.201311050

Cheng EC, Hsieh CL, Liu N, Wang J, Zhong M, Chen T, Li E, Lin H. 2021. The essential function of SETDB1 in homologous chromosome pairing and synapsis during meiosis. *Cell Rep* **34:** 108575. doi:10.1016/j.celrep.2020.108575

Fernandez-Capetillo O, Mahadevaiah SK, Celeste A, Romanienko PJ, Camerini-Otero RD, Bonner WM, Manova K, Burgoyne P, Nussenzweig A. 2003. H2AX is required for chromatin remodeling and inactivation of sex chromosomes in male mouse meiosis. *Dev Cell* **4:** 497–508. doi:10.1016/S1534-5807(03)00093-5

Griffin GK, Wu J, Iracheta-Vellve A, Patti JC, Hsu J, Davis T, Dele-Oni D, Du PP, Halawi AG, Ishizuka JJ, et al. 2021. Epigenetic silencing by SETDB1 suppresses tumour intrinsic immunogenicity. *Nature* **595:** 309–314. doi:10.1038/s41586-021-03520-4

Haeussler M, Schönig K, Eckert H, Eschstruth A, Mianné J, Renaud JB, Schneider-Maunoury S, Shkumatava A, Teboul L, Kent J, et al. 2016. Evaluation of off-target and on-target scoring algorithms and integration into the guide RNA selection tool CRISPOR. *Genome Biol* **17:** 148. doi:10.1186/s13059-016-1012-2

Hasegawa K, Sin HS, Maezawa S, Broering TJ, Kartashov AV, Alavattam KG, Ichijima Y, Zhang F, Bacon WC, Greis KD, et al. 2015. SCML2 establishes the male germline epigenome through regulation of histone H2A ubiquitination. *Dev Cell* **32:** 574–588. doi:10.1016/j.devcel.2015.01.014

Hirota T, Blakeley P, Sangrithi MN, Mahadevaiah SK, Encheva V, Snijders AP, ElInati E, Ojarikre OA, de Rooij DG, Niakan KK, et al. 2018. SETDB1 links the meiotic DNA damage response to sex chromosome silencing in mice. *Dev Cell* **47:** 645–659.e6. doi:10.1016/j.devcel.2018.10.004

Ichimura T, Watanabe S, Sakamoto Y, Aoto T, Fujita N, Nakao M. 2005. Transcriptional repression and heterochromatin formation by MBD1 and MCAF/AM family proteins. *J Biol Chem* **280:** 13928–13935. doi:10.1074/jbc.M413654200

Ichijima Y, Ichijima M, Lou Z, Nussenzweig A, Camerini-Otero RD, Chen J, Andreassen PR, Namekawa SH. 2011. MDC1 directs chromosome-wide silencing of the sex chromosomes in male germ cells. *Genes Dev* **25:** 959–971. doi:10.1101/gad.2030811

Inselman A, Eaker S, Handel MA. 2003. Temporal expression of cell cycle-related proteins during spermatogenesis: establishing a timeline for onset of the meiotic divisions. *Cytogenet Genome Res* **103:** 277–284. doi:10.1159/000076813

Ishiguro KI, Matsuura K, Tani N, Takeda N, Usuki S, Yamane M, Sugimoto M, Fujimura S, Hosokawa M, Chuma S, et al. 2020. MEIOSIN directs the switch from mitosis to meiosis in mammalian germ cells. *Dev Cell* **52:** 429–445.e10. doi:10.1016/j.devcel.2020.01.010

Kojima ML, de Rooij DG, Page DC. 2019. Amplification of a broad transcriptional program by a common factor triggers the meiotic cell cycle in mice. *Elife* **8:** e43738. doi:10.7554/eLife.43738

Li XZ, Roy CK, Dong X, Bolcun-Filas E, Wang J, Han BW, Xu J, Moore MJ, Schimenti JC, Weng Z, et al. 2013. An ancient transcription factor initiates the burst of piRNA production during early meiosis in mouse testes. *Mol Cell* **50:** 67–81. doi:10.1016/j.molcel.2013.02.016

Liu S, Brind'Amour J, Karimi MM, Shirane K, Bogutz A, Lefebvre L, Sasaki H, Shinkai Y, Lorincz MC. 2014. *Setdb1* is required for germline development and silencing of H3K9me3-marked endogenous retroviruses in primordial germ cells. *Genes Dev* **28:** 2041–2055. doi:10.1101/gad.244848.114

Maezawa S, Hasegawa K, Alavattam KG, Funakoshi M, Sato T, Barski A, Namekawa SH. 2018a. SCML2 promotes heterochromatin organization in late spermatogenesis. *J Cell Sci* **131:** jcs217125. doi:10.1242/jcs.217125

Maezawa S, Hasegawa K, Yukawa M, Kubo N, Sakashita A, Alavattam KG, Sin HS, Kartashov AV, Sasaki H, Barski A, et al. 2018b. Polycomb protein SCML2 facilitates H3K27me3 to establish bivalent domains in the male germline. *Proc Natl Acad Sci* **115:** 4957–4962. doi:10.1073/pnas.1804512115

Maezawa S, Sakashita A, Yukawa M, Chen X, Takahashi K, Alavattam KG, Nakata I, Weirauch MT, Barski A, Namekawa SH. 2020. Super-enhancer switching drives a burst in gene expression at the mitosis-to-meiosis transition. *Nat Struct Mol Biol* **27:** 978–988. doi:10.1038/s41594-020-0488-3

Mahadevaiah SK, Turner JM, Baudat F, Rogakou EP, de Boer P, Blanco-Rodríguez J, Jasin M, Keeney S, Bonner WM, Burgoyne PS. 2001. Recombinational DNA double-strand breaks in mice precede synapsis. *Nat Genet* **27:** 271–276. doi:10.1038/85830

Matsui T, Leung D, Miyashita H, Maksakova IA, Miyachi H, Kimura H, Tachibana M, Lorincz MC, Shinkai Y. 2010. Proviral silencing in embryonic stem cells requires the histone methyltransferase ESET. *Nature* **464:** 927–931. doi:10.1038/nature08858

Mochizuki K, Tando Y, Sekinaka T, Otsuka K, Hayashi Y, Kobayashi H, Kamio A, Ito-Matsuoka Y, Takehara A, Kono T, et al. 2018. SETDB1 is essential for mouse primordial germ cell fate determination by ensuring BMP signaling. *Development* **145:** dev164160. doi:10.1242/dev.164160

Namekawa SH, VandeBerg JL, McCarrey JR, Lee JT. 2007. Sex chromosome silencing in the marsupial male germ line. *Proc Natl Acad Sci* **104:** 9730–9735. doi:10.1073/pnas.0700323104

Nicetto D, Zaret KS. 2019. Role of H3K9me3 heterochromatin in cell identity establishment and maintenance. *Curr Opin Genet Dev* **55:** 1–10. doi:10.1016/j.gde.2019.04.013

Peters AH, O'Carroll D, Scherthan H, Mechtler K, Sauer S, Schöfer C, Weipoltshammer K, Pagani M, Lachner M, Kohlmaier A, et al. 2001. Loss of the Suv39h histone methyltransferases impairs mammalian heterochromatin and genome stability. *Cell* **107:** 323–337. doi:10.1016/S0092-8674(01)00542-6

Rowe HM, Friedli M, Offner S, Verp S, Mesnard D, Marquis J, Aktas T, Trono D. 2013. De novo DNA methylation of endogenous retroviruses is shaped by KRAB-ZFPs/KAP1 and ESET. *Development* **140:** 519–529. doi:10.1242/dev.087585

Royo H, Prosser H, Ruzankina Y, Mahadevaiah SK, Cloutier JM, Baumann M, Fukuda T, Höög C, Tóth A, de Rooij DG, et al. 2013. ATR acts stage specifically to regulate multiple aspects of mammalian meiotic silencing. *Genes Dev* **27:** 1484–1494. doi:10.1101/gad.219477.113

Sakashita A, Maezawa S, Takahashi K, Alavattam KG, Yukawa M, Hu YC, Kojima S, Parrish NF, Barski A, Pavlicev M, et al. 2020. Endogenous retroviruses drive species-specific germline transcriptomes in mammals. *Nat Struct Mol Biol* **27:** 967–977. doi:10.1038/s41594-020-0487-4

Saksouk N, Simboeck E, Déjardin J. 2015. Constitutive heterochromatin formation and transcription in mammals. *Epigenetics Chromatin* **8:** 3. doi:10.1186/1756-8935-8-3

Scherthan H, Schöfisch K, Dell T, Illner D. 2014. Contrasting behavior of heterochromatic and euchromatic chromosome portions and pericentric genome separation in pre-bouquet spermatocytes of hybrid mice. *Chromosoma* **123:** 609–624. doi:10.1007/s00412-014-0479-4

Seisenberger S, Andrews S, Krueger F, Arand J, Walter J, Santos F, Popp C, Thienpont B, Dean W, Reik W. 2012. The dynamics of genome-wide DNA methylation reprogramming in mouse primordial germ cells. *Mol Cell* **48:** 849–862. doi:10.1016/j.molcel.2012.11.001

Shao Q, Zhang Y, Liu Y, Shang Y, Li S, Liu L, Wang G, Zhou X, Wang P, Gao J, et al. 2023. ATF7IP2, a meiosis-specific partner of SETDB1, is required for proper chromosome remodeling and crossover formation during spermatogenesis. *Cell Rep* **42:** 112953. doi:10.1016/j.celrep.2023.112953

Soumillon M, Necsulea A, Weier M, Brawand D, Zhang X, Gu H, Barthès P, Kokkinaki M, Nef S, Gnirke A, et al. 2013. Cellular source and mechanisms of high transcriptome complexity in the mammalian testis. *Cell Rep* **3:** 2179–2190. doi:10.1016/j.celrep.2013.05.031

Tan JHL, Wollmann H, van Pelt AMM, Kaldis P, Messerschmidt DM. 2020. Infertility-causing haploinsufficiency reveals TRIM28/KAP1 requirement in spermatogonia. *Stem Cell Reports* **14:** 818–827. doi:10.1016/j.stemcr.2020.03.013

Timms RT, Tchasovnikarova IA, Antrobus R, Dougan G, Lehner PJ. 2016. ATF7IP-mediated stabilization of the histone methyltransferase SETDB1 is essential for heterochromatin formation by the HUSH complex. *Cell Rep* **17:** 653–659. doi:10.1016/j.celrep.2016.09.050

Tsusaka T, Shimura C, Shinkai Y. 2019. ATF7IP regulates SETDB1 nuclear localization and increases its ubiquitination. *EMBO Rep* **20:** e48297. doi:10.15252/embr.201948297

Tsusaka T, Fukuda K, Shimura C, Kato M, Shinkai Y. 2020. The fibronectin type-III (FNIII) domain of ATF7IP contributes to efficient transcriptional silencing mediated by the SETDB1 complex. *Epigenetics Chromatin* **13:** 52. doi:10.1186/s13072-020-00374-4

Turner JM. 2015. Meiotic silencing in mammals. *Annu Rev Genet* **49:** 395–412. doi:10.1146/annurev-genet-112414-055145

van der Heijden GW, Derijck AA, Pósfai E, Giele M, Pelczar P, Ramos L, Wansink DG, van der Vlag J, Peters AH, de Boer P. 2007. Chromosome-wide nucleosome replacement and H3.3 incorporation during mammalian meiotic sex chromosome inactivation. *Nat Genet* **39:** 251–258. doi:10.1038/ng1949

Yeh YH, Hu M, Nakagawa T, Sakashita A, Yoshida S, Maezawa S, Namekawa SH. 2021. Isolation of murine spermatogenic cells using a violet-excited cell-permeable DNA binding dye. *J Vis Exp* **2021:** e61666. doi:10.3791/61666

Yoshida K, Maekawa T, Ly NH, Fujita SI, Muratani M, Ando M, Katou Y, Araki H, Miura F, Shirahige K, et al. 2020. ATF7-dependent epigenetic changes are required for the intergenerational effect of a paternal low-protein diet. *Mol Cell* **78:** 445–458.e6. doi:10.1016/j.molcel.2020.02.028